PAPER

2D solutions of the hyperbolic discrete nonlinear Schrödinger equation

IOP Publishing Physica Scripta
Phys. Scr. 94 (2019) 115203 (10pp) https://doi.org/10.1088/1402-4896/ab2d01

2D solutions of the hyperbolic discrete nonlinear Schrödinger equation

J D'Ambroise[1,3] **and P G Kevrekidis**[2]

[1] Department of Mathematics, Computer & Information Science, State University of New York (SUNY) College at Old Westbury, Westbury, NY 11568, United States of America
[2] Department of Mathematics and Statistics, University of Massachusetts, Amherst, MA 01003, United States of America

E-mail: dambroisej@oldwestbury.edu and kevrekid@math.umass.edu

Received 4 February 2019, revised 29 May 2019
Accepted for publication 26 June 2019
Published 13 August 2019

Abstract

Stationary solutions to the two-dimensional hyperbolic discrete nonlinear Schrödinger equation are derived by starting from the anti-continuum limit and extending solutions to include nearest-neighbor interactions in the coupling parameter. Pseudo-arclength continuation is used to capture the relevant most fundamental branches of localized solutions, and their corresponding stability and dynamical properties (i.e. their fate when unstable) are explored. The focus is on nine primary types of solutions: single site, double site in- and out-of-phase, squares with four sites in-phase and out-of phase in each of the vertical and horizontal directions, four sites out-of-phase arranged in a line horizontally, and two additional solutions having respectively six and eight excited sites. The chosen configurations are found to merge into four distinct bifurcation events. The nature of the bifurcation phenomena is unveiled, typically involving saddle-center collisions and pairwise disappearances of the branches. Finally, the consequences of the termination of the branches on the dynamical phenomenology of the model are explored. When the branches are unstable for small coupling values, they may often dynamically lead into a single site branch. For larger coupling values where no stable branches exist, the solutions are typically found to lead to dispersion involving one or more 'masses' dispersing the energy around a central core.

Keywords: discrete Schrödinger, hyperbolic, nonlinear

(Some figures may appear in colour only in the online journal)

1. Introduction

The hyperbolic nonlinear Schrödinger (HNLS) equation is a model of increasing interest both in applied mathematics and in theoretical/experimental physics [1–6] as it arises in a diverse host of physical applications. Among others, one can mention as specific examples deep water waves [7, 8] and cyclotron waves in plasmas [9, 10], although the equation has been also quite popular in nonlinear optics. Within the latter, the examination of normally dispersive (quasi-discrete) optical waveguide arrays [11, 12] has offered a framework for the study of optical pulses. Additionally, the nonlinear, experimentally accessible X-wave structures [13, 14] (but also more elaborate states including dark-bright [15] or vortex-bright [16] solitary waves) have motivated its theoretical and numerical study. More recent efforts have also seen the development of methods based on hyperbolic coordinates to study the standing waves of the HNLS [17], a consideration of its universal asymptotic regime for a wide range of initial conditions [18], as well as the analysis of its profile decomposition in different mass-critical and supercritical cases [19]; see also references therein. It is relevant to highlight the diversity of recent studies involving this HNLS model. These range over the last decade from nonlinear optics and necking or snaking instabilities [20–22], to water waves and the modeling of rogue or domain wall patterns [23, 24], as well as to the study of nonlinear wave patterns of the model in mathematical physics [25, 26].

While these extensive studies have addressed numerous aspects of the continuum HNLS model, the authors are not

[3] Author to whom any correspondence should be addressed.

aware of any efforts considering the (genuinely) discrete aspects of the model, the so-called hyperbolic discrete nonlinear Schrödinger or HDNLS equation. This is an interesting endeavor on a number of counts. On the one hand, the elliptic variant of the discrete problem is quite well understood (see, e.g., the monograph [27]), hence, it is conceivable that some of the corresponding analytical and numerical techniques may be adapted to the present setting. In fact, there exists a so-called staggering transformation $u_{n,m} = (-1)^n w_{n,m}$ (where $w_{n,m}$ is the solution of the elliptic problem) which can convert the former to the latter. This approach will not be used here, given that this transformation becomes singular in the continuum limit. Instead, notice that the phenomenology of the HDNLS model is of interest not only given its consideration as a numerical scheme for the continuum HNLS, but also because some of the applications may bear a (at least partially) discrete character, as discussed, e.g. in [11, 12].

There are additional characteristics that add to the appeal of the HDNLS model. For instance, in the so-called anti-continuum (AC) limit of vanishing coupling between adjacent nodes, *any* stationary configuration is 'permissible' as is known also for the elliptic case [27]. However, in the continuum limit, on the other hand, the work of [6] established that there are no nontrivial standing wave solutions. This implies that *all* the solutions initiated at the AC limit must terminate at some point prior to reaching the continuum i.e. at some finite value of the coupling strength. This is fundamentally different from the standard elliptic DNLS case, where solitary waves, and even vortical solutions may persist in the continuum limit [1]. It is also a feature that has direct consequences evident in the dynamical evolution of the model for coupling strengths past the critical point of the relevant bifurcations. There, it can be seen that the system is led to dispersional dynamics involving one or more masses depending on the initial condition, as is discussed in detail below. Thus, it is of interest to explore the bifurcations through which these branches terminate and to classify the dynamical behavior of the model prior to, as well as past the corresponding critical points. It is the aim of the present work to address a number of these issues for some of the most fundamental (one- and few-site) configurations of the HDNLS model. The main results are:

- The solvability condition enabling the classification of the stationary states and the characterization of their stability as is adapted from the elliptic case to the hyperbolic one.
- Upon continuation of the principal branches under consideration, four distinct bifurcation events are identified numerically.
- All standing waves are found to disperse for coupling values larger than those of the bifurcation events; for smaller coupling values, they may degenerate to other states, such as most notably the solution involving a single central site.

This analysis is numerically pursued for nine prototypical branches of two-dimensional configurations involving one- and two-site states and the ones connected to the bifurcations and termination of these branches. Understanding these states and how their bifurcations arise provides a set of 'guidelines' for what to expect for larger size configurations.

The presentation will be structured as follows: in section 2, the theoretical aspects of the existence (via solvability conditions) and stability theory (linearizing around the equilibrium configurations and exploring the corresponding spectrum) are explored. Then, numerical computations will be used in section 3 to corroborate the analytical existence/stability results and direct numerical simulations will help determine the fate of such waveforms when unstable (or when they may not exist closer to the continuum limit). Finally, in section 4, the findings are summarized and the conclusions are presented, as well as a number of challenges towards future work.

2. Model

Consider the HDNLS equation for $u_{n,m}(z)$ as follows

$$\mathrm{i}\frac{\mathrm{d}u_{n,m}}{\mathrm{d}z} + \epsilon\,\Delta_H u_{n,m} + |u_{n,m}|^2 u_{n,m} = 0, \tag{1}$$

where $\Delta_H u_{n,m} = u_{n,m+1} + u_{n,m-1} - u_{n+1,m} - u_{n-1,m}$ stands for the hyperbolic operator, i.e. a discretization of $u_{xx} - u_{yy}$ with unit spacing, while ϵ is the nearest neighbor coupling parameter. In the context of this being a (n isotropic) discrete approximation to the continuum problem, one should think of $\epsilon = 1/\Delta x^2$, where Δx is the spacing between adjacent lattice nodes in both directions. The indexing n represents the discrete vertical direction and m the horizontal one. Setting $u_{n,m}(z) = \phi^{(\epsilon)}_{n,m} \mathrm{e}^{\mathrm{i}\mu z}$ gives the stationary equation $F^{(\epsilon)}_{n,m} = 0$ for

$$F^{(\epsilon)}_{n,m}(\phi) \overset{\text{def.}}{=} (\mu - |\phi^{(\epsilon)}_{n,m}|^2)\phi^{(\epsilon)}_{n,m} - \epsilon\,\Delta_H \phi^{(\epsilon)}_{n,m}. \tag{2}$$

One can then seek standing wave solutions with frequency μ, by solving the algebraic set of equations (2). An outline of the workflow associated with the identification of these solutions, their stability, and their implications on the model dynamics is provided in figure 1.

2.1. Existence of solutions

In the $\epsilon = 0$ AC limit, the values of $\phi^{(0)}_{n,m}$ for each site $\{n, m\}$ can be chosen independently from each other since the nearest-neighbor coupling parameter is zero. Localized solutions are thus found by specifying $\phi^{(0)}_{n,m} = 0$ for most sites $\{n, m\}$. For a few nonzero sites one can set $\phi^{(0)}_{n,m} = \mathrm{e}^{\mathrm{i}\theta_{n,m}}$ with $\mu = 1$ and $\theta_{n,m} \in \{0, \pi\}$. Table 1 lists some possible solutions for $\phi^{(0)}_{n,m}$ and a naming convention for each example configuration.

The following general notation will be used. Let $\mathcal{S} = \{\phi^{(0)}_{n_1,m_1}, \phi^{(0)}_{n_2,m_2}, \ldots, \phi^{(0)}_{n_d,m_d}\}$ for $d \in \mathbb{N}$ represent an enumeration of the nonzero sites of the initial $\epsilon = 0$ configuration, and let $\vec{\theta} = \arg(\mathcal{S}) \in [0, 2\pi]^d$ represent a vector whose elements are the arguments of elements of $\mathcal{S}$. For simplicity the nonzero sites are enumerated in a natural way with the top-most left nonzero site corresponding to the first index. Notice that the configurations listed in table 1 are not necessarily closed loops, but when they are they will be enumerated from the top left, continuing counterclockwise. It

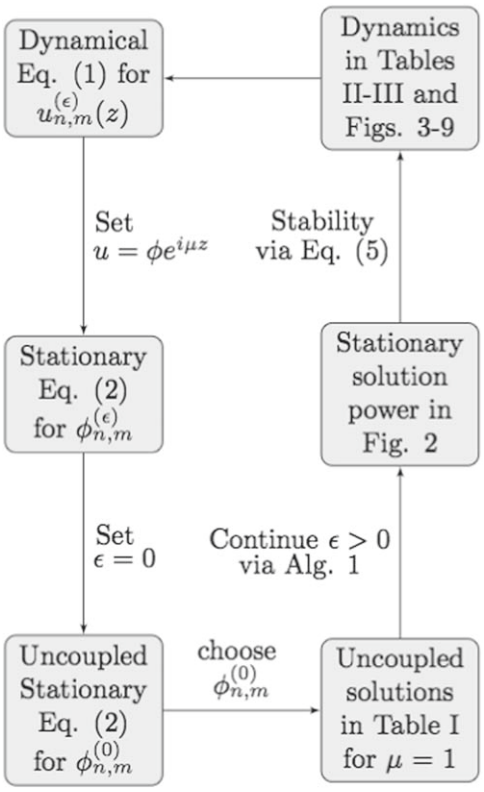

Figure 1. A diagram of the workflow is shown for identifying at $\epsilon = 0$, continuing for $\epsilon > 0$, examining the stability and finally testing the dynamics of the different obtained solutions.

Table 1. Solutions $\phi^{(0)}_{n,m}$ to the stationary equation (2) for $\mu = 1$ are listed with corresponding naming convention for each type. Nonzero sites of the configuration are shown with the values $\phi^{(0)}_{n,m} = \pm 1$ denoted as plus or minus. All other sites are zero. Solutions are grouped by branch number, i.e. according to which ones merge after continuing in ϵ.

Branch 1		Branch 2	
Name	Sites	Name	Sites
1s	+	2o-horz	+ −
2i-horz	+ +	4o-line	+ + − −
4o-vert	+ / + / − / −		

Branch 3		Branch 4	
Name	Sites	Name	Sites
4i-sqr	+ + / + +	4o-horz	− + / − +
8s	− − / + + / + + / − −	6s	+ / − + / − + / +

will be convenient to denote $\vec{\delta}_L$ as a vector whose components are either 0 or 1 corresponding to whether the left neighbor (when considered on the full two-dimensional grid) $\phi^{(0)}_{n_j,m_j-1}$ of each element of $\mathcal{S}$ is zero or nonzero. Similarly define $\vec{\delta}_R$, $\vec{\delta}_T$, $\vec{\delta}_B$ corresponding to whether the right ($\phi^{(0)}_{n,m+1}$), top ($\phi^{(0)}_{n-1,m}$), and bottom ($\phi^{(0)}_{n+1,m}$) neighbors of each element of $\mathcal{S}$ are zero or nonzero on the 2D grid. Finally, let $\vec{\theta}_L, \vec{\theta}_R, \vec{\theta}_T, \vec{\theta}_B \in [0, 2\pi]^d$ denote the arguments of the corresponding nonzero nearest neighbors to each element of $\mathcal{S}$ (with the subscripts having the same neighbor designation as above). Note that since $\mathcal{S}$ contains all of the nonzero elements of $\phi^{(0)}_{n,m}$, the vectors $\vec{\theta}_\star$ are permutations of $\vec{\theta}$.

For $\epsilon > 0$ real-valued solutions $\phi^{(\epsilon)}_{n,m}$ are computed from $\phi^{(0)}_{n,m} \in \mathbb{R}$ via continuation in the coupling parameter ϵ. Such solutions satisfying the limit $\lim_{\epsilon\to 0} \phi^{(\epsilon)}_{n,m} = \phi^{(0)}_{n,m}$ are unique and guaranteed to exist for ϵ in some neighborhood $I_0 = (-\epsilon_0, \epsilon_0)$ by an application of the implicit function theorem. From the stationary equation $F^{(\epsilon)}_{n,m} = 0$ one can directly compute the solvability condition $\mathrm{Im}\,(\phi^{(\epsilon)}_{n,m}\overline{F}^{(\epsilon)}_{n,m}(\phi)) = 0$ where overline represents the complex conjugate. That is, solutions $\phi^{(\epsilon)}_{n,m}$ are also roots of $\vec{g} = [g_{n,m}]$ for elements defined as

$$g_{n,m} = \epsilon\,\mathrm{Im}(\,\phi_{n,m}(\overline{\phi}_{n,m+1} + \overline{\phi}_{n,m-1} - \overline{\phi}_{n+1,m} - \overline{\phi}_{n-1,m})). \tag{3}$$

Considered as a (implicit) function of $\vec{\theta}$ and ϵ, the vector function $\vec{g}$ can be expanded in Taylor series that is convergent on the interval I_0 [27–29]. That is,

$$\vec{g}(\vec{\theta}, \epsilon) = \sum_{k=1}^{\infty} \epsilon^k \vec{g}^{(k)}(\vec{\theta}) \text{ where } \vec{g}^{(k)}(\vec{\theta}) = \frac{1}{k!}\partial^k_\epsilon \vec{g}(\vec{\theta}, 0). \tag{4}$$

Since the initial configuration at $\epsilon = 0$ exhibits a gauge invariance $\vec{\theta} \to \vec{\theta} + \theta_0$ for $\theta_0 \in \mathbb{R}$ this gives a one parameter family of roots of $\vec{g}$ for any fixed $\epsilon \in I_0$. This implies that if the first order Jacobian matrix $J = \partial\vec{g}^{(1)}/\partial\vec{\theta}$ has a simple zero eigenvalue, there exists a unique (modulo gauge transformation) analytic continuation of the limiting solution $\phi^{(0)}$ into the domain I_0 [27–29]. Having provided the conditions for the existence of the different branches of solutions, the next section will address the corresponding spectral stability analysis.

2.2. Spectral stability

For each example solution $\phi^{(\epsilon)}_{n,m}$ in table 1 the stability is monitored for each fixed $\epsilon > 0$ via the linearization ansatz

$$u = \mathrm{e}^{\mathrm{i}\mu z}(\phi^{(\epsilon)}_{n,m} + \delta[a_{n,m}\mathrm{e}^{\nu z} + b^*_{n,m}\mathrm{e}^{\nu^* z}]) \tag{5}$$

which yields the order δ linear system

$$\begin{bmatrix} M_1 & M_2 \\ -M_2^* & -M_1^* \end{bmatrix}\begin{bmatrix} a \\ b \end{bmatrix} = -\mathrm{i}\nu\begin{bmatrix} a \\ b \end{bmatrix}, \tag{6}$$

where $M_1 = \epsilon\Delta - \mu + 2|\phi^{(\epsilon)}|^2$ and $M_2 = (\phi^{(\epsilon)})^2$. Thus $\max(\mathrm{Re}(\nu)) > 0$ corresponds to instability, yielding the relevant instability growth rate, while $\max(\mathrm{Re}(\nu)) = 0$ corresponds to (neutral) stability. Note that $\psi = [a\ b]^T$ represents a column vector of length $2N^2$, where $N \times N$ is the two-dimensional grid size.

In the numerical computations that follow, the relevant solutions are identified via fixed point iterations and

subsequently the matrix eigenvalue problem of equation (6) is solved numerically to determine their stability. However, it is particularly useful to have some theoretical prediction/expectation about which configurations should be expected to be stable and which ones should not. To that effect, the methodology summarized in [27] (based on earlier works such as [30, 31]) is adapted. This allows a connection of the stability of the few-site configurations with the Jacobian of the solvability conditions, as follows.

From equations (4) and using the notation of section 2.1 the bifurcation function is written $\vec{g}^{(1)}$ as follows:

$$\vec{g}^{(1)}(\vec{\theta}) = \vec{\delta}_L \sin(\vec{\theta} - \vec{\theta}_L) + \vec{\delta}_R \sin(\vec{\theta} - \vec{\theta}_R) - \vec{\delta}_T \sin(\vec{\theta} - \vec{\theta}_T) - \vec{\delta}_B \sin(\vec{\theta}_j - \vec{\theta}_B), \quad (7)$$

where the equation is intended to be considered element-wise in each of the excited sites.

Thus the first order Jacobian matrix $J = \partial\vec{g}^{(1)}/\partial\vec{\theta}$ has entries that can be computed manually given any example solution. The diagonal vector of the matrix J is $\delta_L \cos(\theta - \theta_L) + \delta_R \cos(\theta - \theta_R) - \delta_T \cos(\theta - \theta_T) - \delta_B \cos(\theta - \theta_B)$. Non-zero off-diagonal entries are of the form $\pm\cos(\theta_j - \theta_{\star,j})$ where the index of the nonzero entry is the index of nonzero entries of $\delta_\star$ for each of $\star = L, R, T, B$ with the plus sign corresponding to T, B and the minus sign corresponding to L, R. The eigenvalues λ_i of J are then connected to the full stability problem via the relation $\lim_{\epsilon\to 0} \nu_i^2 \big/ \epsilon = 2\lambda_i$, with the relevant proof going through in a same way as with the elliptic case of [27].

The Jacobian matrix for each example configuration that is considered is listed in table 2. Based on the eigenvalues $\{\lambda_i\}$ listed in table 2 the 1s, 2o-horz, and 4o-horz configurations are found to be stable for very small ϵ. For such small ϵ one finds one unstable direction for configurations 2i-horz and 4i-sqr; two for 4o-line and 6s; three for 4o-vert; and six for 8s. Note that adjacent in-phase excitations along the horizontal direction such as 2i-horz, 4i-sqr, and 8s lead to instability, as do out-of-phase excitations in the vertical direction such as 4o-vert. For more complex configurations (like 6s or 8s), whether or not they will bear an instability depends on whether they include such unstable 'base ingredients' i.e. any in phase pair along the horizontal (as is the case for 8s) or out of phase pair along the vertical (as is the case for 6s). Having the analytical predictions of table 2 at hand, the next section will focus on a numerical exploration of the corresponding (potential) instabilities.

Table 2. The table lists the Jacobian matrix J and corresponding eigenvalues $\{\lambda_i\}$ for each configuration. It is important to appreciate that each positive number for λ_i on the right column translates into an unstable pair for the full problem eigenvalues ν_i.

Name	Jacobian J	Eigenvalues $\{\lambda_i\}$
1s	(0)	$\{0\}$
2i-horz	$\begin{pmatrix} 1 & -1 \\ -1 & 1 \end{pmatrix}$	$\{2, 0\}$
4o-vert	$\begin{pmatrix} 2 & -1 & 0 & -1 \\ -1 & 2 & -1 & 0 \\ 0 & -1 & 2 & -1 \\ -1 & 0 & -1 & 2 \end{pmatrix}$	$\{4, 2, 2, 0\}$
2o-horz	$\begin{pmatrix} 1 & -1 \\ -1 & 1 \end{pmatrix}$	$\{-2, 0\}$
4o-line	$\begin{pmatrix} 1 & -1 & 0 & 0 \\ -1 & 0 & 1 & 0 \\ 0 & 1 & 0 & -1 \\ 0 & 0 & -1 & 1 \end{pmatrix}$	$\{2, \pm\sqrt{2}, 0\}$
4i-sqr	$\begin{pmatrix} 0 & 1 & 0 & -1 \\ 1 & 0 & -1 & 0 \\ 0 & -1 & 0 & 1 \\ -1 & 0 & 1 & 0 \end{pmatrix}$	$\{\pm 2, 0, 0\}$
8s	$\begin{pmatrix} 2 & -1 & 0 & 0 & 0 & 0 & 0 & -1 \\ -1 & 1 & 1 & 0 & 0 & 0 & -1 & 0 \\ 0 & 1 & 1 & -1 & 0 & -1 & 0 & 0 \\ 0 & 0 & -1 & 2 & -1 & 0 & 0 & 0 \\ 0 & 0 & 0 & -1 & 2 & -1 & 0 & 0 \\ 0 & 0 & -1 & 0 & -1 & 1 & 1 & 0 \\ 0 & -1 & 0 & 0 & 0 & 1 & 1 & -1 \\ -1 & 0 & 0 & 0 & 0 & 0 & -1 & 2 \end{pmatrix}$	$\{4, 2 \pm \sqrt{2}, 2, 2, \pm\sqrt{2}, 0\}$
4o-horz	$\begin{pmatrix} -2 & 1 & 0 & 1 \\ 1 & -2 & 1 & 0 \\ 0 & 1 & -2 & 1 \\ 1 & 0 & 1 & -2 \end{pmatrix}$	$\{-4, -2, -2, 0\}$
6s	$\begin{pmatrix} 1 & -1 & 0 & 0 & 0 & 0 \\ -1 & -1 & 1 & 0 & 1 & 0 \\ 0 & 1 & -2 & 1 & 0 & 0 \\ 0 & 0 & 1 & -2 & 1 & 0 \\ 0 & 1 & 0 & 1 & -1 & -1 \\ 0 & 0 & 0 & 0 & -1 & 1 \end{pmatrix}$	$\{-3.681\,33, -1.642\,07, \pm\sqrt{3}, 0\ 1.323\,4\}$

3. Numerical results: existence, stability and dynamics

In the appendix there is a short pseudocode algorithm for the arclength continuation procedure that is utilized in order to identify the relevant branches of solutions numerically. The continuation is initiated at $\epsilon = 0$ with the various solutions listed in table 1. The power of the resulting solutions $P(\epsilon) = \sum_{n,m} |\phi_{n,m}^{(\epsilon)}|^2$ is plotted as a function of $\epsilon > 0$ in figure 2. The figure shows that the power curves merge into four bifurcation 'events'. The branch labels are indicated in the caption of figure 2 as ordered from lowest to highest power. Dashed lines represent unstable solutions and solid ones represent stable solutions. Branch 1 (lowest power) exists up to the value of $\epsilon \approx 0.242$ where solutions originating from types 1s, 2i-horz, and 4o-vert meet. Branch 2 (lower middle) exists up to $\epsilon \approx 0.226$ at which point the solutions originating from types 2o-horz and 4o-line meet. Branch 3 (upper middle) exists up to $\epsilon \approx 0.210$ where types 4i-sqr and 8s meet. Branch 4 (highest power) exists up to $\epsilon \approx 0.251$ where types 4o-horz and 6s meet.

In figures 3–6 the sample solutions $\phi_{n,m}^{(\epsilon)}$ on the left columns show typical branch members while the result of the two-dimensional continuation procedure over ϵ is shown on the right panel through the unstable eigendirection growth rates $\mathrm{Re}(\nu)$. Comparing table 1 to the left columns of figures 3–6 it is found that the extended solutions originate from the $\epsilon = 0$ solutions in the following manner as the nearest neighbor interaction is turned on for $\epsilon > 0$. Generally

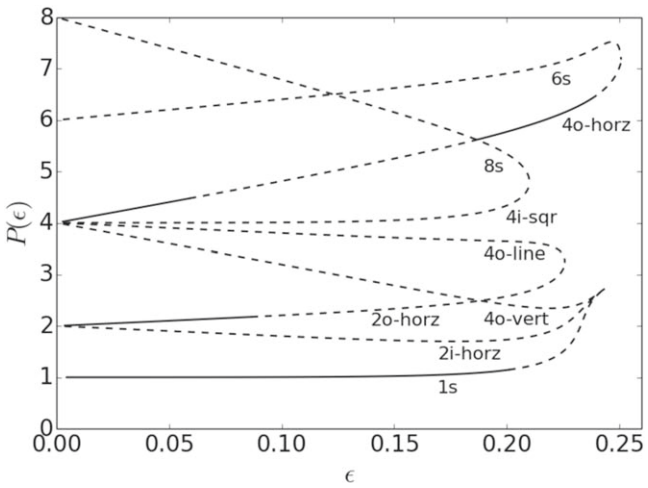

Figure 2. The power $P(\epsilon) = \sum_{n,m} |\phi^{(\epsilon)}_{n,m}|^2$ of solutions to the stationary equation (2), obtained by arclength continuation, plotted as a function of $\epsilon > 0$. Underneath each branch segment is a label representing the $\epsilon = 0$ configuration from which the solution is continued.

sites to the left and right of the initial configuration become nonzero with the same sign as the initial configuration, and sites neighboring the initial configuration vertically become nonzero with opposite sign as the initial configuration. Signs of the sites then alternate vertically and stay the same horizontally in a manner that respects the signs of the initial configuration as the footprint continues to expand for increasing $\epsilon > 0$.

Solutions initiated at $\epsilon = 0$ from the configuration types of 1s, 2i-horz, and 4o-vert merge into a single branch denoted as Branch 1. These three solution types merge at $\epsilon \approx 0.242$ and the left column of figure 3 shows example solutions for $\epsilon = 0.2414$ on Branch 1. In the right column of figure 3 the nonzero real parts of eigenvalues ν are plotted as computed from equation (6). Note that the eigenvalue plots denote real eigenvalues with an 'x' mark and nonreal complex eigenvalues with an 'o' mark. For very small ϵ the prediction $\nu \approx \sqrt{2\lambda\epsilon}$ from section 2.2 is plotted in a red dashed line based on the values of λ in table 2. Clearly, the one unstable eigenvalue of the 2i-horz configuration and the two unstable eigenvalues of the 4o-vert configuration are well captured for small ϵ. As ϵ increases, however, these real eigenvalue pairs appear to turn around towards $\nu = 0$ and tend the origin of the spectral plane as the bifurcation point is approached.

One can follow the eigenvalue diagrams in figure 3 with the following description of the change of the eigenvalue types as a function of ϵ. Starting with the 1s configuration, near the merging point there is one nonzero real pair of eigenvalues within the range $0.201 \leqslant \epsilon \leqslant 0.241$. Near the merge point this one real pair of eigenvalues moves towards the origin. Additionally two pairs of eigenvalues on the imaginary axis tend toward the origin (these are not reflected in figure 3). The 2i-horz has one nonzero real pair for $0 < \epsilon \leqslant 0.211$ and two real pairs for $0.212 \leqslant \epsilon \leqslant 0.241$. Near the merge point the two real pairs and one additional

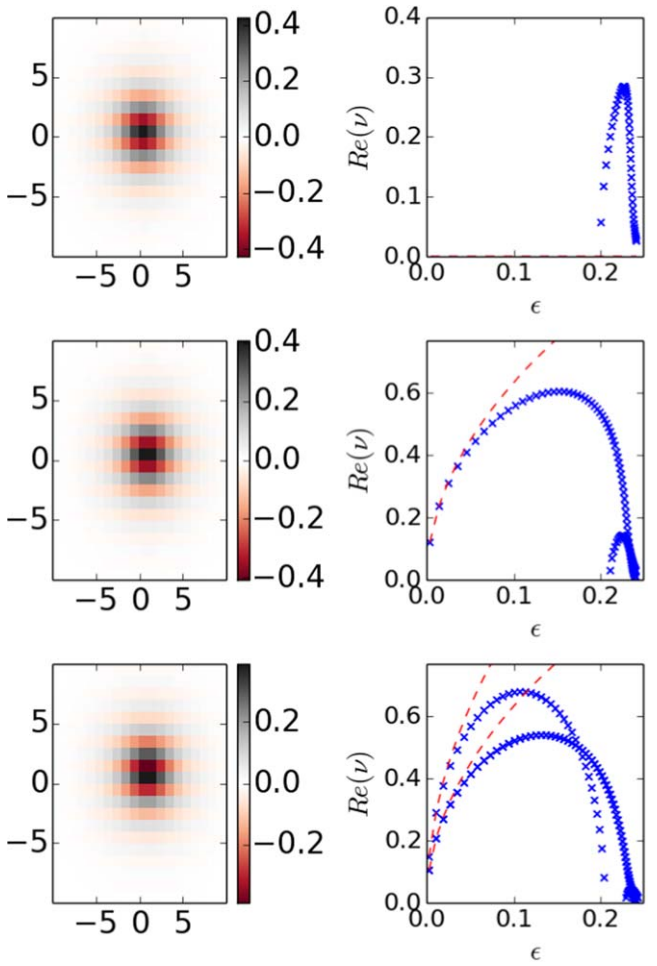

Figure 3. Each configuration plotted in the left column shows a Branch 1 (real-valued) solution that was obtained by continuation of the coupling parameter to the value of $\epsilon = 0.2414$ where the original configuration at $\epsilon = 0$ is 1s (top), 2i-horz (middle), or 4o-vert (bottom). In the right column the set of values $\{\mathrm{Re}(\nu) > 0\}$ is plotted for the corresponding whole branch segment versus ϵ where similarly the original configuration at $\epsilon = 0$ is 1s (top), 2i-horz (middle), or 4o-vert (bottom). For the right column, circles mark the values for which $\mathrm{Im}(\nu) > 0$ (i.e. ν is complex non-real and existing as quartets in the complex plane) and x's mark the values for which $\nu \in \mathbb{R}$ (i.e. ν is real and existing as pairs on the real axis of the complex plane).

imaginary pair approach the origin. The 4o-vert has initially a total of three nonzero real pairs (one pair coinciding for a total of two distinct) within the range $0 < \epsilon \leqslant 0.205$, then within the range $0.206 \leqslant \epsilon \leqslant 0.229$ two real pairs, and the remaining interval $0.230 \leqslant \epsilon \leqslant 0.241$ again three nonzero pairs (one pair coinciding, two distinct). Nearest to the merge point the three real eigenvalues decrease in amplitude towards the origin.

Solutions initiated at $\epsilon = 0$ from the configurations types 2o-horz and 4o-line merge at $\epsilon \approx 0.226$ as Branch 2. Figure 4 shows example solutions for $\epsilon = 0.2258$ on the left column. Note that according to table 2 the 2o-horz type is initially (i.e. for small ϵ) stable and the 4o-line type initially has two unstable directions for small ϵ. The predictions $\nu \approx \sqrt{2\lambda\epsilon}$

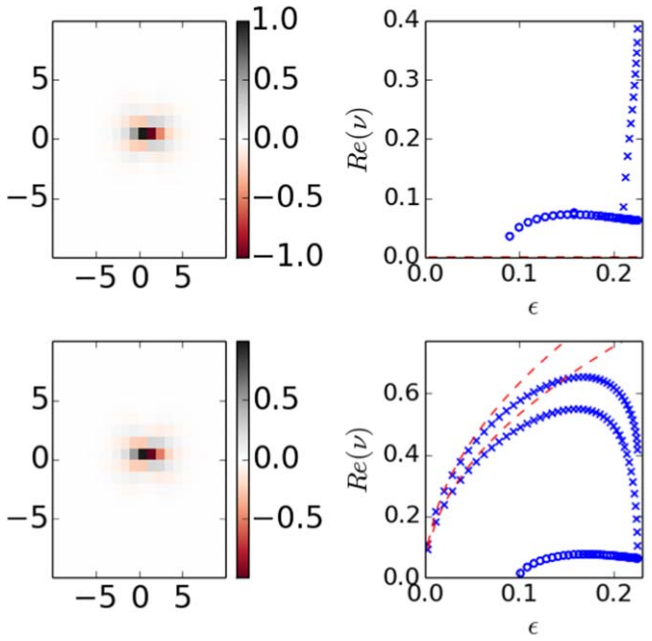

Figure 4. Plots are similar to figure 3 but here for Branch 2 with the left column corresponding to $\epsilon = 0.2258$ with initial $\epsilon = 0$ configurations here as 2o-horz (top row) and 4o-line (bottom row).

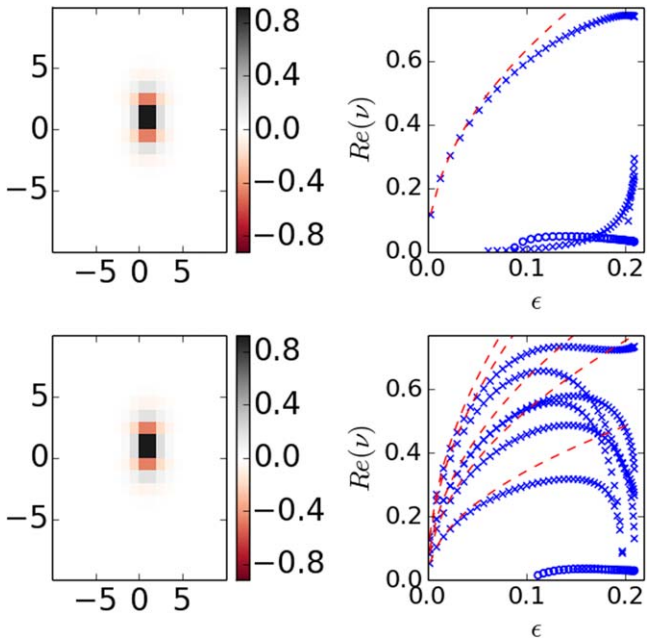

Figure 5. Plots are similar to figure 3 but here for Branch 3 with the left column corresponding to $\epsilon = 0.2101$ with initial $\epsilon = 0$ configurations here as 4i-sqr (top row) and 8s (bottom row).

according to table 2 are plotted as red dashed lines in the right column of figure 4. For small ϵ, the two unstable eigendirections of 4o-line are well captured. As ϵ is increased, in the right column one can follow the eigenvalue changes over ϵ. The 2o-horz type has one quartet with nonzero real part within the range $0.083 \leqslant \epsilon \leqslant 0.225$ and then within the range $0.210 \leqslant \epsilon \leqslant 0.225$ there is an additional real pair. The 4o-line type has two real pairs for $0 < \epsilon \leqslant 0.225$ and an additional quartet for $0.101 \leqslant \epsilon \leqslant 0.225$. Near the merge

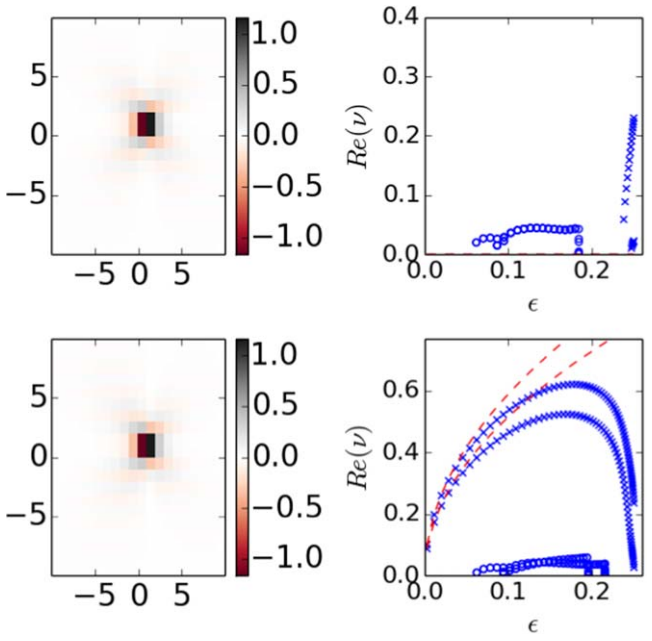

Figure 6. Plots are similar to figure 3 but here for Branch 4 with the left column corresponding to $\epsilon = 0.2509$ with initial $\epsilon = 0$ configurations here as 4o-horz (top row) and 6s (bottom row).

point for Branch 2 the magnitude of the real parts of the quartet eigenvalues from both the 2o-horz and the 4o-line approach approximately 0.05 as $\epsilon \to 0.226$. The merge point also has one real pair with magnitude approximately 0.38. Notice that the 2o-horz type has the real pair *increasing* toward this value while the 4o-line type has its largest real pair *decreasing* toward this value (the smaller real pair for 4o-line type goes to zero). Moreover, to confirm the saddle-center nature of this bifurcation, the 2nd real pair of the 4o-line branch decreases towards the origin $\nu = 0$ as the bifurcation point is approached, while the 2o-horz branch has an imaginary eigenvalue pair (not shown here) tending to collide with this real pair (of 4o-line) at the origin.

Solutions initiated from 4i-sqr and 8s merge at $\epsilon \approx 0.210$ as Branch 3 and figure 5 shows example solutions for $\epsilon = 0.2101$. Note that according to table 2 the 4i-sqr type has one unstable direction and 8s has six unstable directions for small ϵ. These predictions are plotted as red dotted lines in the right column of figure 5, again in good agreement with the numerical results at least for small values of ϵ, before turning around towards $\nu = 0$, which in this case too happens around $\epsilon = 0.1$. The eigenvalue types change over ϵ as follows. The type 4i-sqr has a real pair for $0 < \epsilon \leqslant 0.210$, a second real pair for the interval $0.056 \leqslant \epsilon \leqslant 0.210$ and a third real pair for the interval $0.203 \leqslant \epsilon \leqslant 0.210$. Note also that a quartet appears in the interval $0.088 \leqslant \epsilon \leqslant 0.210$. The type 8s has six real pairs for most of the ϵ range with two persisting for the smaller interval $0 < \epsilon \leqslant 0.199$ and four persisting (two overlapping) for the whole interval $0 < \epsilon \leqslant 0.210$. Additionally a quartet exists for $0.108 \leqslant \epsilon \leqslant 0.210$. On both types 4i-sqr and 8s the largest real pair approaches a magnitude of approximately 0.73 as $\epsilon \to 0.2101$ and the complex quartet has the magnitude of its real part approaching 0.02. On both

Table 3. The table lists the fate of solutions obtained via continuation in ϵ when they are propagated in the variable z according to the dynamical equation (1).

	$\mathrm{Im}(\nu)=0$	$\mathrm{Im}(\nu)\neq 0$	$\mathrm{Im}(\nu)=0$	$\mathrm{Im}(\nu)\neq 0$
	$\epsilon=0.1500$		$\epsilon=0.2250$	
1s	(stable)	—	1 m	—
2i-horz	1s	—	1s-trans	—
4o-vert	1s	—	1s-trans	—
	$\epsilon=0.1500$		$\epsilon=0.2096$	
2o-horz	—	1s	2 m	1–2 m
4o-line	1s	1s	1s-trans	1s-trans
	$\epsilon=0.1500$			
4i-sqr	1s	1s		
8s	1s	1s		
	$\epsilon=0.1500$		$\epsilon=0.2400$	
4o-horz	—	1s	4 m	—
6s	1s	1s	4 m	—

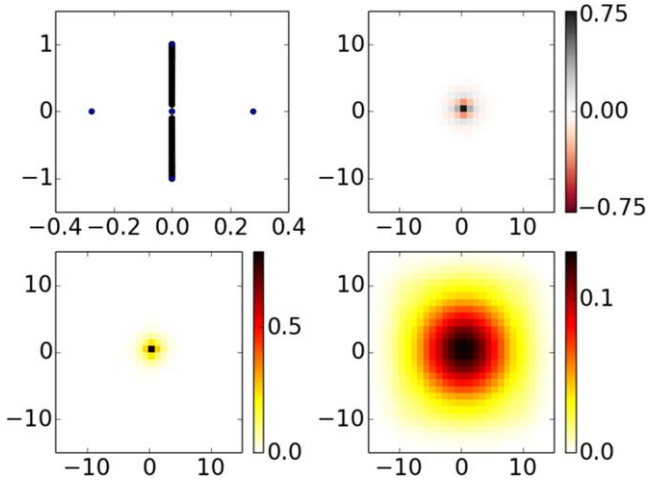

Figure 7. The top left panel shows the values $\{\nu\}$ plotted in the complex plane for the corresponding stationary solution $\phi^{(\epsilon)}_{n,m}$ that is plotted in the top right panel. The solution at $z=0$ is of type 1s for $\epsilon=0.2250$ and it is real-valued, and $|a+b^*|$ corresponding to the eigenvalue ν that has largest real part is plotted in the bottom left panel. After propagating the result $|\phi^{(\epsilon)}_{n,m}(z)|$ is plotted in the bottom right for $z=50$.

types 4i-sqr and 8s, focusing on the smaller real pairs of eigenvalues, they approach a magnitude of either 0.24 or 0.31. Notice that the 8s configuration has at this point two extra real pairs (the overlapping pair) unaccounted for thus far —they approach zero as the merge point nears. These are the eigenvalues responsible for this saddle-center bifurcation, while the 4i-sqr branch has two corresponding pairs tending to $\nu=0$ from the imaginary side.

Solutions initiated from 4o-horz and 6s merge at $\epsilon\approx 0.251$ as Branch 4 in the final example among our saddle-center bifurcations. Figure 6 shows example solutions for $\epsilon=0.2509$. Table 2 predicts that 4o-horz is initially stable and 6s initially has two unstable directions. The 4o-horz type has one complex quartet for $0.059\leqslant\epsilon\leqslant 0.082$ and three such for $0.083\leqslant\epsilon\leqslant 0.096$ (two coinciding), while two coinciding ones remain for $0.097\leqslant\epsilon\leqslant 0.185$. Near $\epsilon=0.185$ these complex eigenvalues rapidly return to the imaginary axis. A real pair of eigenvalues exists close to the merging point in the interval $0.237\leqslant\epsilon\leqslant 0.251$ and a second real pair appears very near that merge point for $0.248\leqslant\epsilon\leqslant 0.251$. The 6s type has two real pairs of eigenvalues for $0<\epsilon\leqslant 0.251$ and an additional quartet for $0.061\leqslant\epsilon\leqslant 0.091$ and a total of three quartets for $0.092\leqslant\epsilon\leqslant 0.102$; then, it has a total of two quartets for $0.103\leqslant\epsilon\leqslant 0.197$ and one quartet for $0.198\leqslant\epsilon\leqslant 0.217$. Near $\epsilon=0.217$ the quartets of eigenvalues rapidly return to the imaginary axis. Near the merging point for Branch 4 the magnitudes of the two real pairs of eigenvalues *decrease* towards the limiting magnitude value of 0.02 and 0.23 as $\epsilon\to 0.251$ for the 6s configuration while the two real pairs of eigenvalues on the 4o-horz side of the branch *increase* towards those same magnitude values as $\epsilon\to 0.251$. Thus, in the vicinity of this point, the two configurations collide and merge through the associated turning point of this final saddle-center bifurcation.

In table 3 the dynamical fate of some case example solutions is listed together with the type of the perturbing eigenvectors. Solutions are initiated at $z=0$ according to equation (5) with $\delta=0.001$ and with eigenvector $[a\ b]^T$ corresponding to the eigenvalue ν that has largest real part where ν is either real (denoted as $\mathrm{Im}(\nu)=0$) or in the complex plane with nonzero imaginary part ($\mathrm{Im}\,(\nu)\neq 0$). One circular mass is denoted as 1m such as the bottom right panel of figure 7, two expanding masses is denoted as 2m such as the middle right panel of figure 8, four masses expanding towards the corners of the grid is denoted as 4m such as the bottom right panel of figure 9, and 1–2m corresponds to one mass expanding in one direction and a smaller mass in the opposite direction such as the bottom right panel of figure 8. The abbreviation 1s-trans represents a transient state that is a pulsating 1s type.

The 1s type solution at $\epsilon=0.2250$ evolves towards a single expanding mass marked as 1m in the table. Figure 7 shows the original solution at $z=0$ in the top right panel and the evolved solution at a later z value in the bottom right panel. The corresponding maximal eigenvalues in the top left panel are defined according to equations (5) and (6). The eigenvector is in the bottom left panel. The eigenvector $[a\ b]^T$ corresponding to the positive real ν value is used to perturb the solution according to equation (5). The result of the evolution propagated according to equation (1) in the bottom right panel clearly illustrates the dispersive nature of the temporal dynamics.

Table 3 shows that at $\epsilon=0.2096$ the solution of type 2o-horz has two different fates depending on whether one perturbs according to (5) in the eigendirection corresponding to the maximal real eigenvalue (marked as the $\mathrm{Im}(\nu)=0$ column of the table) versus the other eigendirection corresponding to the maximal complex eigenvalue (marked as the Im $(\nu)\neq 0$ column of the table). In the former case the 2o-horz

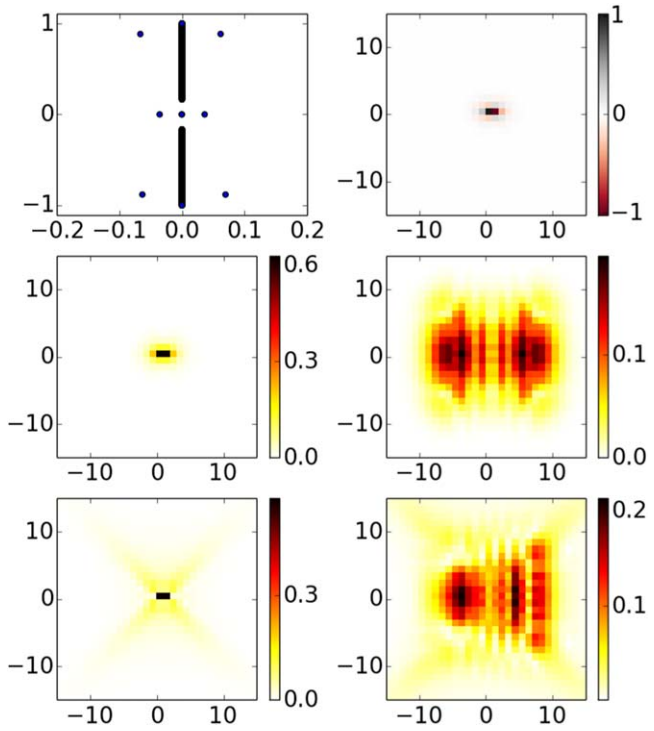

Figure 8. Plots are similar to figure 7 where the top right panel shows the real-valued solution of type 2o-horz at $z = 0$ for $\epsilon = 0.2096$. The middle left panel shows $|a + b^*|$ corresponding to the eigenvalue with maximum real part among the quartet of eigenvalues (with Im $(\nu) \neq 0$). Perturbing with this eigenvector results in solution $|\phi^{(\epsilon)}_{n,m}(z)|$ in the middle right panel plotted at $z = 218$. The bottom row of panels is similar but for the eigenvector corresponding to the real eigenvalue with maximum real part among the real eigenvalues (with Im$(\nu) = 0$). The resulting solution $|\phi^{(\epsilon)}_{n,m}(z)|$ is in the bottom right panel at $z = 122$.

type solution evolves towards an expanding mass with two 'blobs' moving outwards along the horizontal direction; this is marked as 2m in the table and shown in the middle right panel of figure 8 with the corresponding eigenvector shown in the middle left panel. In the latter case such expansion is not symmetric—this is marked as 1–2m in the table and shown in the bottom right panel of figure 8 with the corresponding eigenvector shown in the bottom left panel. Apparently here the perturbation added on top of the initial 2o-horz configuration breaks its symmetry, leading to the asymmetric evolution of the bottom right of figure 8.

For other configurations such as 4o-line, 4i-sqr and 8s, according to table 3, their instabilities typically led to a single-site resulting evolution for the values of ϵ-considered (for which the single site configuration was dynamically stable). In the cases of 2i-horz and 4o-vert for $\epsilon = 0.225$, the configurations approach a transient 1s state, vibrating near a 1s type solution with a pulsating core, since the stationary 1s configuration is unstable for this value of ϵ. On the other hand, at $\epsilon = 0.2400$ the 4o-horz and 6s configurations evolve with mass expanding mostly towards the four corners, as is demonstrated in figure 9. Indeed, all other solutions shown in table 3 revert towards the 1s type, i.e. disperse mass while

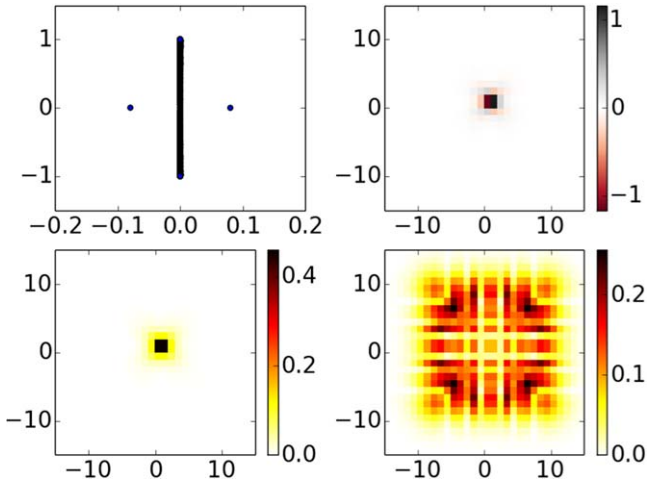

Figure 9. Plots are similar to figure 7 where the top right panel shows the real-valued solution of type 4o-horz at $z = 0$ for $\epsilon = 0.2400$. The middle left panel shows $|a + b^*|$. Perturbing according to (5) with this eigenvector results in the solution $|\phi^{(\epsilon)}_{n,m}(z)|$ plotted in the bottom right panel at $z = 116$.

transforming to a single site excited configuration. Solutions on Branches 1–4 are tested when propagated according to equation (1) with ϵ beyond the bifurcation points such as $\epsilon = 0.28$, 0.3 to find that all tested standing wave solutions disperse for such higher ϵ values, closer to the continuum limit. This is in line with the expectation that no coherent structure exists in the vicinity of the continuum limit. Yet, our quantitative analysis illustrates that dispersion dominates already for rather weak couplings i.e. $\epsilon > 0.25$. Whether a discrete analogue of self-similar dynamics arises for this interval (corresponding to the continuum observations of [18]) is an interesting open question for future study.

4. Conclusions and future challenges

In the present work, some of the fundamental solutions of the hyperbolic discrete nonlinear Schrödinger model are explored. The search for such waveforms was initiated at the convenient AC limit and continuation in the coupling parameter was used for some of the most prototypical ones, most notably one-, two- and four-site examples, with some exceptions involving six- and eight-site examples, when these were participating in bifurcations involving the lower number of site branches. The solvability condition methodology of the elliptic case was adapted to this hyperbolic case and existence conditions were accordingly derived as well as predictions for the eigenvalues of the linearization of such few-site configurations. Subsequently, the states were obtained via fixed point iterations and the validity of the analytics as a function of the coupling strength ϵ was examined. It was generally found that the eigenvalue predictions worked well in the vicinity of the AC limit. However, at larger values of the coupling (typically of $\approx$0.2), the eigenvalues were found in many configurations to 'turn around' and either meet up with

a merging segment of the branch or return to the origin leading to a set of bifurcation patterns that were elucidated herein, some in fact involving more than 2 configurations (as was the case with the branches 1s, 2i, 4o-vert). This aligns itself with our expectation that *all* standing wave solutions disappear in the continuum limit [6]. Sufficiently beyond these critical bifurcation thresholds (all of which satisfied $0.2 \leqslant \epsilon_{\rm cr} \leqslant 0.25$ for the examples considered), the fate of standing wave-like initial conditions was also examined and it was found that they disperse, forming one or more dispersing 'blobs', depending on the form of the initial condition. Interestingly, this type of fate (of dispersion into one or multiple blobs) could arise for select examples before the bifurcation critical points, as elaborated in table 3. Nevertheless, in numerous cases of the latter scenario, the configurations just rearranged themselves towards eventually reaching a single site state (1s).

Naturally, the present work paves the way for the numerous intriguing questions both at the theoretical and at the numerical level. A difficult set of questions concerns the phenomenology around $\epsilon_{\rm cr}$. Our analysis enables an understanding for small ϵ; is there, however, a way to capture the 'turning' of the eigenvalues or the emergence of these bifurcations around these critical values of ϵ? Beyond these critical values, does one encounter a discrete variant of the universal regimes presented in [18] and if so is there a way to analyze such phenomenology at the discrete level ? Finally, extending considerations to the three-dimensional setting with two directions bearing the same sign of the dispersion (diffraction, at the discrete level) and one the opposite would be a possibility of interest in its own right. Some of the questions are presently under consideration and will be reported in future publications.

Acknowledgments

The authors acknowledge early efforts in this direction by Dr Kai Li PGK is also grateful to Profs. MJ Ablowitz and Boris A Malomed for illuminating discussions on the subject. This material is based upon work supported by the National Science Foundation under Grant No. DMS-1809074 (PGK). JDA gratefully acknowledges computing support based on the Army Research Office ARO-DURIP Grant W911NF-15-1-0403.

Appendix

In algorithm 1 an initial solution $\phi^{(0)}_{n,m}$ for $\epsilon_0 = 0$ from table 1 is assumed to be represented as a column vector of length N^2, where $N \times N$ is the size of the two-dimensional grid. The function $F(\phi, \epsilon) = F_\epsilon(\phi)$ is defined according to equation (2) and also outputs a column vector of length N^2. The constant values of the change in arclength parameter ds, the maximum ϵ value $\epsilon_{\rm max}$, and the tolerance are assumed to be pre-set.

Algorithm 1. Arclength continuation.

$\epsilon_0 = 0$; $\phi_0 = \phi^{(0)}$;
$v = \text{nullspace}\left(\left[\frac{\partial F}{\partial \phi}(\phi_0, \epsilon_0) \;\; \frac{\partial F}{\partial \epsilon}(\phi_0);\right]\right)$;
$v = v/\text{norm}(v)$; ▷ initial direction vector
do
  $\phi = \phi_0$; $\epsilon = \epsilon_0$;
  do ▷ Newton's method on augmented function G
    $D = [\phi;\, \epsilon;\,] - [\phi_0;\, \epsilon_0;\,]$;
    $G = [F(\phi, \epsilon);\, D \cdot v - ds;\,]$;
    $M = \left[\frac{\partial F}{\partial \phi}(\phi_0, \epsilon) \;\; \frac{\partial F}{\partial \epsilon}(\phi);\, v^T;\right]$
    $corr = M \backslash G$;
    $[\phi;\, \epsilon;\,] = [\phi;\, \epsilon;\,] -$ corr;
  while norm(corr) > tolerance
  $v = \left[\frac{\partial F}{\partial \phi}(\phi_0, \epsilon) \;\; \frac{\partial F}{\partial \epsilon}(\phi);\, v^T;\right] \backslash [zeros(N^2, 1);\, 1;]$;
  $v = v/\text{norm}(v)$; ▷ next direction vector
  $\phi_0 = \phi$; $\epsilon_0 = \epsilon$;
while $\epsilon < \epsilon_{\rm max}$

ORCID iDs

J D'Ambroise https://orcid.org/0000-0001-9301-7853
P G Kevrekidis https://orcid.org/0000-0002-7714-3689

References

[1] Sulem C and Sulem P L 1999 *Nonlinear Schrödinger Equations: Self-Focusing And Wave Collapse* (*Applied Mathematical Sciences* vol 139) (Berlin: Springer)
[2] Conti C, Di Trapani P and Trillo S 2009 *Self-Focusing: Past and Present—Fundamentals and Prospects* (*Topics in Applied Physics* vol 114) (Berlin: Springer) p 439
[3] Conti C and Trillo S 2008 *Localized Waves* ed H E Hernandez-Figueroa *et al* (Hoboken, NJ: John Wiley and Sons Inc) p 243
[4] Ghidaglia J M and Saut J C 1990 *Nonlinerity* **3** 475
[5] Ghidaglia J M and Saut J C 1993 *J. Nonlinear Sci.* **3** 169
[6] Ghidaglia J M and Saut J C 1996 *J. Nonlinear Sci.* **6** 139
[7] Ablowitz M and Segur H 1979 *J. Fluid Mech.* **92** 691–715
[8] Zakharov V and Kuznetsov E 2012 *Phys.—Usp.* **55** 535
[9] Pereira N, Sen A and Bers A 1978 *Phys. Fluids* **21** 117
[10] Myra J and Liu C 1980 *Phys. Fluids* **23** 2258
[11] Droulias S, Hizanidis K, Meier J and Christodoulides D N 2005 *Opt. Express* **13** 1827
[12] Lahini Y, Frumker E, Silberberg Y, Droulias S, Hizanidis K, Morandotti R and Christodoulides D 2007 *Phys. Rev. Lett.* **98** 023901
[13] Conti C, Trillo S, Di Trapani P, Piskarkas A, Jedrkiewicz O and Trull J 2003 *Phys. Rev. Lett.* **90** 170406
[14] Di Trapani P, Valiulis G, Piskarkas A, Jedrkiewiecz O, Trull J, Conti C and Trillo S 2003 *Phys. Rev. Lett.* **91** 093904
[15] Hayata K and Koshiba M 1993 *Phys. Rev.* E **48** 2312
[16] Efremidis N, Hizanidis K, Malomed B and Di Trapani P 2007 *Phys. Rev. Lett.* **98** 113901
[17] Kevrekidis P, Nahmod A R and Zeng C 2011 *Nonlinearity* **24** 1523
[18] Ablowitz M J, Ma Y-P and Rumanov I 2017 *SIAM J. Appl. Math.* **77** 1248
[19] Dodson B, Marzuola J L, Pausader B and Spirn D 2018 *Illinois J. Math.* **62** 293

[20] Gorza S-P, Deconinck B, Emplit P, Trogdon T and Haelterman M 2011 *Phys. Rev. Lett.* **106** 094101
[21] Gorza S-P, Deconinck B, Emplit P, Trogdon T and Haelterman M 2012 *Opt. Lett.* **37** 4657
[22] Cisneros-Ake L A, Carretero-González R, Kevrekidis P G and Malomed B A 2019 *Commun. Nonlinear Sci. Numer. Simul.* **74** 268
[23] Ruban V 2015 *J. Exp. Theor. Phys.* **120** 925
[24] Tsitoura F, Gietz U, Chabchoub A and Hoffmann N 2018 *Phys. Rev. Lett.* **120** 224102
[25] Ai-Lin G and Ji L 2010 *Commun. Theor. Phys.* **54** 401
[26] Lu N 2015 *Discr. Contin. Dyn. Sys.* **35** 3533
[27] Kevrekidis P G 2009 *The Discrete Nonlinear Schrödinger Equation: Mathematical Analysis, Numerical Computation and Physical Perspectives* (Heidelberg: Springer)
[28] Chow S N and Hale J K 1982 *Methods of Bifurcation Theory* (Heidelberg: Springer)
[29] Golubitsky M and Schaeffer D G 1985 *Singularities and Groups in Bifurcation Theory* (vol 1) (New York: Springer)
[30] Pelinovsky D E, Kevrekidis P G and Frantzeskakis D J 2005 *Physica* D **212** 1
[31] Pelinovsky D E, Kevrekidis P G and Frantzeskakis D J 2005 *Physica* D **212** 20